PCCP

ROYAL SOCIETY OF CHEMISTRY

PAPER

View Article Online
View Journal | View Issue

Cite this: *Phys. Chem. Chem. Phys.*, 2023, **25**, 4997

Aluminium ion doping mechanism of lithium thiophosphate based solid electrolytes revealed with solid-state NMR†

Hongtao Qu,‡[a] Yantao Wang,‡[bc] Jiangwei Ju,[b] Ernst R. H. van Eck,*[a] Guanglei Cui*[bc] and Arno P. M. Kentgens*[a]

We investigate the impact of Al incorporation on the structure and dynamics of Al-doped lithium thiophosphates ($Li_{3-3x}Al_xPS_4$) based on β-Li_3PS_4. ^{27}Al and ^{6}Li magic-angle spinning NMR spectra confirm that Al^{3+} ions occupy octahedral sites in the structure. Quantitative analyses of ^{27}Al NMR spectra show that the maximum Al incorporation is x = 0.06 in $Li_{3-3x}Al_xPS_4$. The ionic conductivity of β-Li_3PS_4 is enhanced by over a factor 3 due to Al incorporation. Further increase of the Al doping level leads to the formation of a more complicated material consisting of multiple crystalline and distorted phases as indicated by ^{31}P NMR spectra and powder X-ray diffraction. Consequently, novel Li ion diffusion pathways develop leading to a very high ionic conductivity at room temperature. NMR relaxometry shows that the activation barrier for long-range Li ion diffusion in β-Li_3PS_4 hardly changes upon Al incorporation, but the onset temperature for motional narrowing comes down significantly due to Al doping. The activation barrier in the subsequently formed multiphase material decreases significantly, however, indicating a different more efficient Li ion conduction pathway.

Received 7th October 2022,
Accepted 16th January 2023

DOI: 10.1039/d2cp04670a

rsc.li/pccp

1. Introduction

All-solid-state lithium batteries (ASSLBs) are recognized as promising next generation energy storage systems as they have the potential to provide higher energy density and assured safety.[1,2] To realize this, a lot of work has been done to develop high ion-conductive solid electrolytes. A variety of electrolytes have been investigated, including oxides, sulphides, halides, *etc.*[3,4] Among these, thio-LISICON (LIthium SuperIonic CONductor) families with a general formula of $Li_xM_{1-y}M'_yS_4$ (M = Ge, Si, Sn, *etc.* M′ = P, Ga, Al, Zn, *etc.*) are of great interest due to their high ionic conductivity, reaching 10^{-4}–10^{-2} S cm^{-1} at ambient temperature which is comparable, or even superior, to the performance of liquid electrolytes.[5,6]

Li ion diffusion within solids is usually governed by the presence of Li defects, *i.e.* vacancies and/or interstitials. The number of mobile species and vacancies determines the ionic conductivity.[7] Aliovalent substitution is an easy but effective way to modify certain materials. Ions of the host structure are replaced by ions of a different valence, introducing additional vacancies or interstitials elsewhere in the structure to preserve electroneutrality.[8] According to this rule, thio-LISICON families are derived from Li_4GeS_4 *via* various cation substitutions at the Ge^{4+} site.[6,9,10] For instance, partial replacement of Ge^{4+} by P^{5+} (Ge^{4+} + Li^+ → P^{5+}) creates vacancies in the Li sub-lattice and generates a class of solid ion conductors with extremely high ionic conductivity: $Li_{4-x}Ge_{1-x}P_xS_4$ (LGPS), including $Li_{3.25}Ge_{0.75}P_{0.25}S_4$ (2.2 mS cm^{-1} at 25 °C) and $Li_{3.33}Ge_{0.33}P_{0.67}S_4$ (commonly known as $Li_{10}GeP_2S_{12}$, 12 mS cm^{-1} at 25 °C).[6,11] Unfortunately, the high cost and chemical instability of germanium renders the application of LGPS impractical.[12,13]

Al doping has been widely used in oxide electrolytes to stabilize the structure and enhance the Li ionic conductivity since aluminium is abundant and stable.[14–18] Fig. 1 displays the crystal structure of β-Li_3PS_4 and several building blocks such as PS_4^{3-}, $P_2S_6^{4-}$, and $P_2S_7^{4-}$ which are commonly observed in the lithium thiophosphate family.[19,20] β-Li_3PS_4 has an orthorhombic structure characterized by space group *Pnma* (No. 62). It consists of isolated PS_4^{3-} tetrahedra. Li ions are distributed over 3 types of Wyckoff sites, namely, tetrahedral Li1 (8d), octahedral

[a] *Magnetic Resonance Research Center, Institute for Molecules and Materials, Radboud University, Heyendaalseweg 135, 6525 AJ Nijmegen, The Netherlands. E-mail: a.kentgens@nmr.ru.nl, e.vaneck@nmr.ru.nl*
[b] *Qingdao Industrial Energy Storage Research Institute, Qingdao Institute of Bioenergy and Bioprocess Technology, Chinese Academy of Sciences, Qingdao 266101, People's Republic of China. E-mail: cuigl@qibebt.ac.cn*
[c] *School of Future Technology, University of Chinese Academy of Sciences, Beijing 100049, People's Republic of China*

† Electronic supplementary information (ESI) available. See DOI: https://doi.org/10.1039/d2cp04670a

‡ These authors contributed equally.

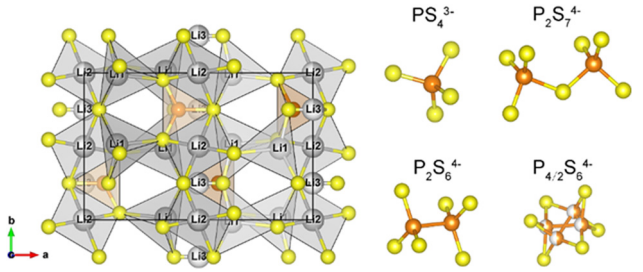

Fig. 1 Crystal structure of β-Li_3PS_4 and some common P–S units in Li_2S–P_2S_5 binary system. The crystal structure is created by VESTA.[26] The Li, P, and S atoms are represented by grey, orange, and yellow spheres, respectively. The half orange P atoms indicate that only the diagonal P sites can be occupied simultaneously.

Li2 (4b) and tetrahedral Li3 (4c) with site occupancies of 1.0, 0.66 and 0.34, respectively. Li ion diffusion in β-Li_3PS_4 is highly anisotropic along the *b* axis *via* the 4b–4c sites as these sites are not fully occupied, *i.e.* contain many vacancies facilitating Li hopping.[21–23]

Previous studies of amorphous Li–Al–P–S systems showed that the addition of Al can induce a structural transformation.[24] To the best of our knowledge, the effects of incorporating Al on the Li ion dynamics and structure of crystalline β-Li_3PS_4 has not been explored in the literature. In this paper, we focus on understanding the Al ion doping mechanism and Li ion dynamics using solid-state NMR spectroscopy focussing in particular on the Al incorporation in β-Li_3PS_4 and the structural development of the samples as a function of Al addition. We perform $^{6/7}$Li, ^{27}Al and ^{31}P NMR to explore Al incorporation in β-Li_3PS_4 to establish the relationship between Li ion dynamics and the structure of the Al-doped materials. It is found that Al dopants occupy octahedral Li2 (4b) sites, introducing vacancies at the Li1 (8d) sites which are fully occupied in pristine β-Li_3PS_4. Therefore, Li ion jumps between *bc* planes are facilitated. Only part of the Al from the Al_2S_3 precursor enters the β-Li_3PS_4 system. We also show that the addition of Al induces further structural evolution, forming multiphasic material consisting of both crystalline and amorphous components that substantially facilitate Li ion transport. The electrochemical characterization of these hetero-nanodomains of $Li_{3-3x}Al_xPS_4$ and $Li_7P_3S_{11}$ and their grain boundaries and the demonstration of their effectiveness in solid-state batteries is described in a separate publication.[25]

2. Experimental

2.1. Synthesis of Al-doped LPS samples

All synthesis procedures were carried out in a high purity argon atmosphere to prevent the material from reacting with moisture and oxygen. The starting materials, Al_2S_3 (MACKLIN, ≥99%), P_2S_5 (MACKLIN, ≥99%), Li_2S (Alfa Aesar, 99.9%), were mixed in an Ar-filled glovebox with target ratios tabulated in Table 1. The mixtures were sealed hermetically into a zirconia jar and ball-milled for 24 h at a speed of 450 rpm using a high energy planetary ball-milling apparatus (Fritsch, Pulverizette 7). After ball-milling, the powders were compressed into pellets and then transferred into an air-tight tube furnace. The compressed pellets were sintered at 300 °C for 8 h under Ar atmosphere and then cooled down to room temperature. Samples are identified as LPS*XY* where *X* and *Y* are the percentage of Li_2S and P_2S_5 in the mixture. The amount of Al incorporated in the Li_3PS_4 structure is expressed as *x* for the phase with a structure formula of $Li_{3-3x}Al_xPS_4$.

2.2. Electrochemical impedance spectroscopy

Electrochemical impedance spectroscopy (EIS) was conducted on a Biologic VMP-300 electrochemical workstation over a frequency range of 7 MHz to 100 mHz with 50 mV voltage perturbation. The samples for solid-state NMR measurements were obtained by grinding the pellets from the same batch into even and fine powders.

2.3. Powder X-ray diffraction measurements

Powder XRD spectra were collected on a Bruker-AXS Micro diffractometer (D8 ADVANCE) using Cu Kα radiation (1.5406 Å). The scanning speed is 0.02° per step within the range of 2θ = 10°–70°.

2.4. Solid-state NMR spectroscopy

Variable-temperature static ^{7}Li solid-state NMR spectra were recorded on a Varian VNMRS system operating at a magnetic field strength of 9.4 T (Larmor frequency: 155.46 MHz for ^{7}Li) with a 5 mm Gonio static probe. The sample was packed under N_2 atmosphere in a glovebox and sealed air-tightly. Spin–lattice T_1 relaxation (SLR) was measured using saturation-recovery pulse sequence. A locking-field of 38.8 kHz was used for spin–lattice relaxation measurement in the rotating frame. ^{6}Li MAS NMR measurements were perform at a magnetic field of 9.4 T (58.86 MHz for ^{6}Li) using a 4 mm MAS HXY Chemagnetics probe. The sample was packed into 4 mm zirconia rotors and spun at 5 kHz. Solid-state ^{27}Al and ^{31}P NMR experiments were performed using a Varian VNMRS spectrometer operating at 19.96 T (^{31}P Larmor frequency of 344.09 MHz, ^{27}Al Larmor frequency of 221.48 MHz). All ^{27}Al and ^{31}P MAS NMR spectra were collected using a HXY triple resonance probe with 1.6 mm zirconia MAS rotors. For ^{27}Al NMR measurements, an "Al-free" rotor was used. The rotor was spun at 32 kHz and 20 kHz for ^{27}Al and ^{31}P MAS NMR measurement, respectively. To obtain quantitative ^{27}Al NMR spectra, a 2.7 μs pulse length equivalent to a 30 degree flip angle with a recycle delay of 30 s was used. ^{31}P MAS NMR spectra were recorded using 90° pulse of 3 μs length and a recycle delay of 50 s. ^{27}Al MQMAS spectra were acquired using a three pulse sequence with a z-filter. The first two hard pulses for triple quantum coherence excitation and conversion are 2.5 μs and 0.8 μs at an RF strength between 120–130 kHz, respectively. The third soft detection pulse was 8 μs in length at an rf field strength of about 10 kHz. ^{27}Al-{^{31}P} rotational-echo, double-resonance (REDOR) NMR experiments were performed at a spin rate of 10 kHz. The spin echo pulse sequence was applied on ^{27}Al nuclei. Meanwhile, rotor-synchronized π pulses were applied on the ^{31}P nuclei. Signals

Table 1 Nomenclature, stoichiometric molar ratio of precursors for Al-doped LPS samples and their room-temperature ionic conductivities

Sample	Li_2S	P_2S_5	Al_2S_3	σ (mS cm^{-1})
LPS7525	75	25	0	0.2
LPS7426	74	26	4/3	0.64
LPS7327	73	27	8/3	3.30
LPS7228	72	28	12/3	13.2
LPS7129	71	29	16/3	1.43
LPS7030	70	30	20/3	0.33
LPS6931	69	31	24/3	0.03
LPS6535	65	35	40/3	0.01

with (S^0) and without (S) ^{31}P irradiation were recorded with increasing the number (N) of rotor cycles. The signal attenuation is normalized as $\Delta S/S^0 = (S^0 - S)/S^0$. Then, the REDOR build-up curve was obtained through plotting $\Delta S/S^0$ as a function of dipolar recoupling time ($N \times T_r$, T_r is the duration of one rotor period). $^{6/7}$Li, ^{27}Al and ^{31}P chemical shifts are respectively referenced to LiCl solution, $AlCl_3$ solution and 85% H_3PO_4. All spectra are processed using the ssNake processing software.[27]

3. Results and discussion

3.1. Ionic conductivity of Al-doped LPS

The ionic conductivities were determined using impedance spectroscopy (Table 1).[25] The pristine LPS7525, *i.e.* β-Li_3PS_4, has an ionic conductivity of 0.2 mS cm^{-1} which is comparable to the values reported in the literature.[21–23] With increasing Al content, ionic conductivities rise accordingly. A maximum value of 13.2 mS cm^{-1} is observed for LPS7228. The ionic conductivity drops dramatically when the Al content is further increased, implying that there is an optimal composition for Li ion transport. The Nyquist plots of all the samples are displayed in Fig. S1 (ESI†). A typical Nyquist plot consisting of a semicircle and a spike is observed for LPS7525. It is hard to separate bulk and grain boundary conductivity. They are distinguishable only when Li ion motions in bulk and grain boundary respond at different frequencies. In our cases, the overall resistance can be extracted from the EIS measurement. Upon Al incorporation, the overall resistance is reduced drastically in LPS7426. Further Al incorporation leads to liquid-like conductivity in LPS7327 and LPS7228. In order to understand the origin of the enhanced ionic conductivities, we need to gain in-depth insights into the structure and Li ion dynamics at different length scale, *i.e.* at both macroscopic and microscopic level.

3.2. Structural evolutions in Al-doped LPS

The overall crystal structures of the synthesized Al-doped LPS series were firstly checked with powder X-ray diffraction measurements. The PXRD patterns of LPS samples with different compositions are presented in Fig. S2 (ESI†). Before the Al^{3+} ions are introduced into the host framework, a pure β-Li_3PS_4 is obtained. Upon increasing the Al^{3+} content, no obvious changes are observed in the PXRD patterns of LPS7426. When the Al^{3+} doping level is further increased, several distinct reflections appear in the 2θ range of 20°–25° and 30°–55°, which is indicative

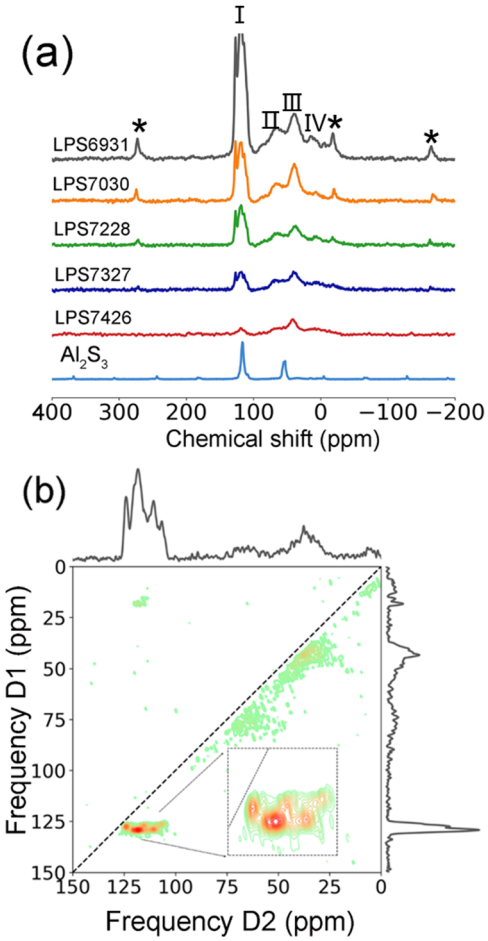

Fig. 2 (a) ^{27}Al MAS NMR spectra of Al-doped LPS series, (b) ^{27}Al 3QMAS spectrum of LPS7228. Spinning sidebands were marked with asterisk. Through the ^{27}Al 3QMAS spectrum, we can confirm that the peaks in region I are the superposition of three peaks.

of the structural changes. The LPS6931 and LPS6535 samples exhibit a lower crystallinity as evidenced by the significant line broadening of their diffraction lines.

^{31}P NMR chemical shifts are used as the indicators to discriminate different polyanionic frameworks in the materials. Fig. S3 (ESI†) displays the 1D ^{31}P MAS NMR spectra for samples LPS7525, LPS7228 and LPS7030. Clearly the LPS system undergoes structural evolutions. In the spectrum of LPS7525 (β-Li_3PS_4), only isolated PS_4^{3-} polyhedral at 87 ppm are present.[28] When adding Al, $P_2S_7^{4-}$ units at 91 ppm appear which are considered to be part of the highly conducting Li7P3S11 electrolyte.[29] The appearance of $P_2S_7^{4}$-indicates that there is an upper limit of the Al solubility in β-Li_3PS_4. It is worth noting that a substantial amount of $P_2S_6^{4-}$ units (104 and 108 ppm) are found in LPS7030 which could be the reason for the collapse of ionic conductivity at higher Al doping levels.[30]

To study the local environment of Al in the prepared samples, ^{27}Al MAS NMR spectra were collected as shown in Fig. 2a. On initial inspection we observe a great number of (partially) overlapping resonances. For further analyses we decide to divide the spectrum in 4 spectral regions denoted

as I, II, III, IV. Firstly, we have to mention that peaks at around 16 ppm in region IV are due to some oxidized impurities and/or signal from the rotor. Although we used Al-reduced zirconia rotors, there is still a tiny amount of Al present in the rotor material. The ^{27}Al NMR spectrum of an empty Al-reduced rotor is presented in Fig. S4 (ESI†), showing signal at around 16 ppm. The resonance lines above 100 ppm in region I are attributed to 4-fold coordinated Al in AlS_4 polyhedra. This region clearly contains a superposition of several resonances that can be assigned to AlS_4 polyhedra in various polymorphs of Al_2S_3.[31]

The signals in region IIII and III fall in the regimes of pentahedral and/or octahedral sulphur-coordinated Al sites.[32,33] Based on a comparison with the ^{27}Al NMR spectrum of the precursor, Al_2S_3, it is concluded that the peaks in region I and II are due to Al_2S_3 remaining in the sample, however, the typical reflection peaks for Al_2S_3 are not visible in the XRD patterns. We do observe a broadening of the diffraction peaks, hinting that the Al_2S_3 is significantly distorted as a result of the ball-milling procedure. This was verified using 2D ^{27}Al MQMAS spectroscopy that is able to separate overlapping peaks on the basis of their difference in chemical shift and/or quadrupolar interaction. Fig. 2b presents the MQMAS spectrum of the LPS7228 sample. Obviously, the signals in region I are the summation of multiple peaks which can be well resolved in the isotropic F1 dimension. In addition, we acquired 1D ^{27}Al MAS NMR spectra at different magnetic fields (Fig. S5, ESI†). Going from 14.09 T to 19.96 T, we observe a decreasing line width for the resonances in region I. While the line width of signals in region II and III have a similar line width at both fields indicating that the resonances are affected by both a distribution in chemical shift and the quadrupolar interaction as the chemical shift is proportional to the magnetic field and the second-order inversely proportional, the combination of both can add up to give a similar line width at different fields. The MQMAS spectrum confirms this interpretation.

To establish which aluminium sites have phosphorus in their direct vicinity, ^{27}Al–{^{31}P} REDOR experiments were performed on sample LPS7030. Fig. 3a shows the ^{27}Al REDOR spectra with varying ^{31}P recoupling time. What can be clearly seen is that only peaks in region III show signal attenuation due to the dipolar recoupling, pointing out the proximity of these Al atoms to P atoms in the structure. Fig. 3b presents the ^{31}P magnetization dephasing profile. Since the REDOR fraction, defined as $\Delta S/S^0 = 1 - S/S^0$, approaches 1, all these Al are close to P.[34] The REDOR spectra of LPS7228 show similar behaviour as shown in Fig. S6 (ESI†). It is interesting that only the Al sites resonating at around 39 ppm are in close proximity to phosphorus atoms. Considering the structure of β-Li_3PS_4 containing isolated PS_4^{3-} polyhedra, the Al ions are most likely substituted in the vacant sites in β-Li_3PS_4 as the octahedral 4b and the tetrahedral 4c sites in the crystal structure are not fully occupied. It is worth to note that the chemical shifts of resonances in region III correspond to aluminium in an octahedral sulphur coordination.

To gain insight in the substitution mechanism, ^{6}Li MAS NMR experiments were performed on β-Li_3PS_4, LPS7426 and LPS7228, respectively. Room temperature ^{6}Li MAS NMR spectra of β-Li_3PS_4 and LPS7228 can be found in Fig. 4. Both spectra are characterized by a single resonance at 0.85 and 0.75 ppm, respectively. In β-Li_3PS_4, three Li sites occur in the structure, namely, Li1 (8d), Li2 (4b) and Li3 (4c), which should occur at a ratio of approximately 20 : 7 : 3 based on the site occupancies.[21] Stöffler *et al.* reported a ^{6}Li MAS NMR spectrum of β-Li_3PS_4 showing two separate peaks for different Li sites at room temperature.[22] In the β-Li_3PS_4 in this study, obtained by mechanosynthesis, all three Li sites are involved in exchange at room temperature or even lower temperature, resulting in a single ^{6}Li peak. Due to this fast exchange of Li between these lattice sites on the NMR time scale, only a single exchange-averaged resonance is observed at room temperature. Variable temperature experiments show that site exchange of Li ions over all sites already starts at 173 K (Fig. 4). The difference in the ^{6}Li MAS NMR spectrum in this study and the work of Stöffler *et al.* may be due to the different synthesis procedure.[35]

In Fig. 3c the low temperature spectrum of β-Li_3PS_4, the spectrum shows two resonance lines located at 1.14 ppm and 0.56 ppm with an intensity ratio of approximately 2 : 1 (see deconvolution in Fig. S7, ESI†), based on this intensity ratio we assign the 1.14 ppm resonance to Li1 whereas the Li2 and Li3 resonances are thought to overlap at 0.56 ppm. The peak at 1.14 ppm reduces in relative intensity upon increasing the Al content, implying Al incorporation in the lattice leads to a reduction of Li in the Li1 (8d) sites. Combined with the results of the ^{27}Al NMR, we postulate that Al atoms occupy vacant octahedral Li2 (4b) sites, as a result, to maintain charge balance, vacancies are created in the Li1 (8d) sites, hence the reduction in relative intensity of the resonance at 1.14 ppm.

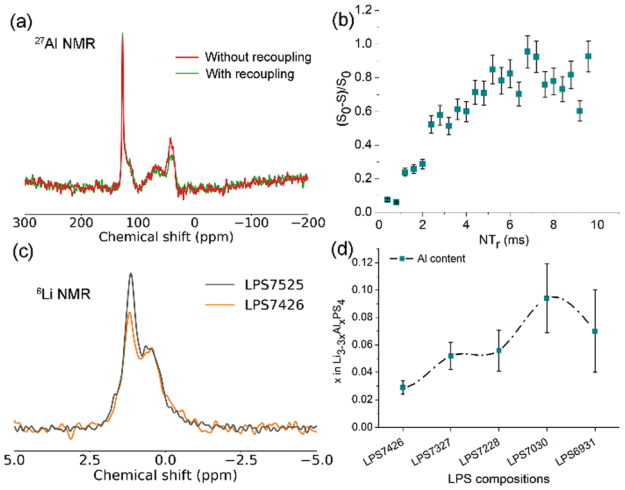

Fig. 3 (a) ^{27}Al (^{31}P) REDOR spectra of LPS7030 with increasing rotor periods (T_r), (b) REDOR build-up curve. In ^{27}Al (^{31}P) REDOR experiments, the signal attenuation of the ^{27}Al resonance at 39 ppm is caused by the dipolar recoupling to nearby ^{31}P. (c) ^{6}Li MAS NMR spectra measured at 153 K and 133 K, for LPS7525 and LPS7426, respectively. For LPS7525, we can observe the well-resolved ^{6}Li spectrum at 153 K, while for the doped sample, we have to go lower temperature to freeze out Li ion motions since the mobility is enhanced by Al incorporation, (d) Al content in the Al-doped $Li_{3-3x}Al_xPS_4$.

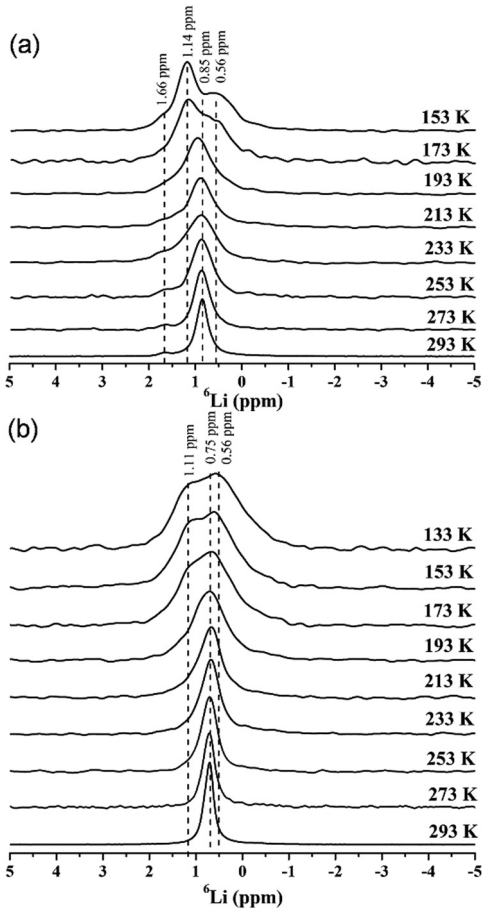

Fig. 4 Variable-temperature ^{6}Li MAS spectra of (a) β-Li_3PS_4 and (b) LPS7228.

To quantify the incorporation of Al in β-Li_3PS_4, we go back to the 1D ^{27}Al MAS NMR spectra displayed in Fig. 2a. We applied a short 30° pulse to ensure quantitative excitation of all the Al sites in the sample. Table S1 (ESI†) summarizes the integrals of region I, II, III, and IV. Based on that, we can calculate the amount of Al dopants that are doped into the structure in $Li_{3-3x}Al_xPS_4$ from the relative ratios of different regions (Fig. 3d). It should be noted again that only Al resonances in region III are from Al in $Li_{3-3x}Al_xPS_4$. Based on the intensities of the different regions in the Al spectrum, the maximum amount of Al incorporation in β-Li_3PS_4 is found to be around 0.06, which has also been reported for Al-doped Argyrodite solid electrolytes, probably due to the smaller ionic radius of Al^{3+} (0.535 Å) compared to Li^+ (0.76 Å).[36] Further increase of Al content causes the formation of multiple crystalline and disorder, which is confirmed in the PXRD patterns and ^{31}P MAS NMR spectra.[25] The formation mechanism of LPS7228 sample was investigated by *in situ* XRD, cryo-TEM and DFT calculations which is described in a separate paper.[25] *In situ* XRD measurements confirms the sequential crystallization process. $Li_{2.82}Al_{0.06}PS_4$ crystallizes initially as the core and $Li_7P_3S_{11}$ grows on the surface of $Li_{2.82}Al_{0.06}PS_4$ which is observed by TEM. When the Al incorporation level is further increased, in LPS7030 and LPS6931 samples, there exist huge amount of $Li_4P_2S_6$ and unreacted Al_2S_3 which cause the collapse in Li ion conductivity.

3.3. Li ion dynamics

Fig. 5a and b display the static ^{7}Li spectra of the β-Li_3PS_4 and LPS7426 samples while the spectra for the LPS7327 and LPS7228 can be found in Fig. S8 (ESI†). At first sight, all of the spectra display similar characteristics and trends as the temperature rises. At 143 K, a broad base is seen in the range from −20 to +20 kHz which originates from the satellite transitions of the quadrupolar ^{7}Li (I = 3/2) nuclear spins. Since the ^{7}Li nucleus is a half-integer spin with relatively small quadrupolar moment, the energy levels of ^{7}Li are only perturbed by first-order quadrupolar interactions, *i.e.* the central transition is hardly affected by quadrupolar couplings but broadened by the dipolar interactions with neighbouring spins. The featureless line shape of the satellite transitions is attributed to a broad distribution of the electric field gradient over all ^{7}Li sites in the lattice. On top of the satellites, a dipolar broadened central transition is visible. Upon increasing the temperature, motional narrowing (MN) sets in; the Li ion motions, *i.e.* site exchange between Li1 and Li2 as well as Li3 sites, speed up and exceed the rigid-lattice linewidth, hence the lines narrow. At room temperature, clear quadrupolar features are visible in the line shape for β-Li_3PS_4 corresponding to a mean quadrupolar coupling constant of ∼35 kHz, whereas these features are smeared out in the doped samples due to the increased structural disorder leading to a distribution in quadrupolar couplings caused by Al incorporation.

The changes in the line shape of the static ^{7}Li spectra as a function of temperature are more or less a universal behaviour of fast Li ion conductors.[37] The linewidth is extracted from the central line and plotted against temperature. As can be seen in

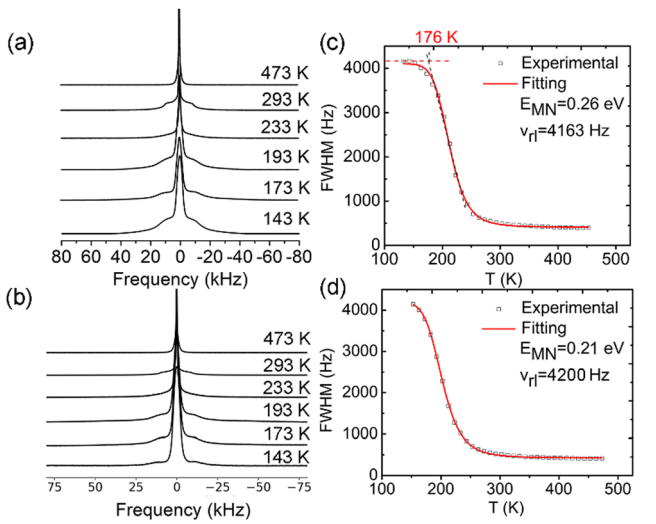

Fig. 5 Selected variable-temperature (VT) static ^{7}Li spectra of (a), β-Li_3PS_4 and (b), LPS7426. Corresponding linewidth of the central transition extracted from the ^{7}Li static spectra for (c) β-Li_3PS_4 and (d) LPS7426, respectively.

Fig. 5c and d, the linewidth reaches a maximum of ~4 kHz in the rigid-lattice regime where the Li ion mobility is too slow to affect the linewidth, $\Delta\nu_{rl}$. As the temperature rises, motional narrowing is clearly observed until the Li ion hopping rates exceed the line width $1/\tau_{MN} \geq 2\pi\Delta\nu_{rl}$. We estimate the onset temperature (T_{onset}) of the motional narrowing from the inflections in the curve of the linewidth as a function of temperature. Upon increasing the Al doping, the onset temperature for the motional narrowing process shifts to lower temperature. For instance, the motional narrowing process starts at 166 K for LPS7426, which is attributed to enhanced Li ion exchange between Li1 and Li2/Li3 sites. Then the hopping rates τ_{MN}^{-1} can be determined at T_{onset} since $1/\tau_{MN} = 2\pi\Delta\nu_{rl}$.[7,38–41] It should be noted that the motional narrowing process starts at much lower temperature in LPS7228 than in β-Li_3PS_4, indicating enhanced Li ion mobility. Finally, the linewidth reaches a plateau, where the homonuclear ^{7}Li–^{7}Li dipolar interaction is averaged out due to the fast Li ion hopping. This motional narrowing process is thermally activated and therefore obeys the Arrhenius equation: $\tau_{MN}^{-1} = \tau_0^{-1}\exp(-E_{MN}/(k_BT))$. Empirically, the linewidth evolution can be fitted by the phenomenological equation proposed by Hendrickson and Bray,[42] from which we can obtain the activation energy for motional narrowing and the rigid-lattice linewidth.

Parameters extracted from the fitting are listed in Table 2. Based on these, the average correlation time for Li ion motions at 298 K is calculated to be 3.5×10^{-8} s for β-Li_3PS_4. According to the Einstein–Smoluchowski equation, the diffusion coefficient D is related to the jumping distance and jumping rates using the formula $D = a^2/2d\tau$, where a is the mean squared displacement and d is the dimensionality.[43,44] In β-Li_3PS_4, we assume that a is the shortest distance over which the Li ion can hop (~3.15 Å). For 3D diffusion, this would yield a diffusion coefficient $D = 4.7 \times 10^{-13}$ m^2 s^{-1}. In general, the ionic conductivity σ_{NMR} can be estimated using the Nernst–Einstein equation: $\sigma_{NMR} = (DN_{Li}e^2)/(k_BT)$,[22,41,45] where $N_{Li} = 1.8 \times 10^{28}$ m^{-3} is the number of Li ions per unit volume, $e = 1.602 \times 10^{-19}$ C is the elementary charge, $k_B = 1.38 \times 10^{-23}$ J K^{-1} is the Boltzmann constant and T is the temperature in Kelvin. Bringing these values into the formula, $\sigma_{NMR} = 0.53$ mS cm^{-1} which is much higher than the experimental value.

Another way of gaining insights into ^{7}Li ion mobility is through spin–lattice relaxation time measurements. Variable temperature ^{7}Li relaxation rates R_1 and $R_{1\rho}$ collected for all samples are shown in Fig. 6. The temperature dependence of R_1

Table 2 Parameters derived for the best-fits of motional narrowing process

Compositions	E_{MN} (eV)	$\Delta\nu_{rl}$ (Hz)	T_{onset} (K)	τ_0^{-1} (s^{-1})
β-Li_3PS_4	0.26	4163 ± 26	176 ± 2	7.1×10^{11}
LPS7426	0.22	4200 ± 16	166 ± 2	1.3×10^{11}
LPS7327	0.22	4050 ± 43	151 ± 2	5.5×10^{11}
LPS7228	0.23	4050 ± 54	143 ± 2	3.3×10^{12}

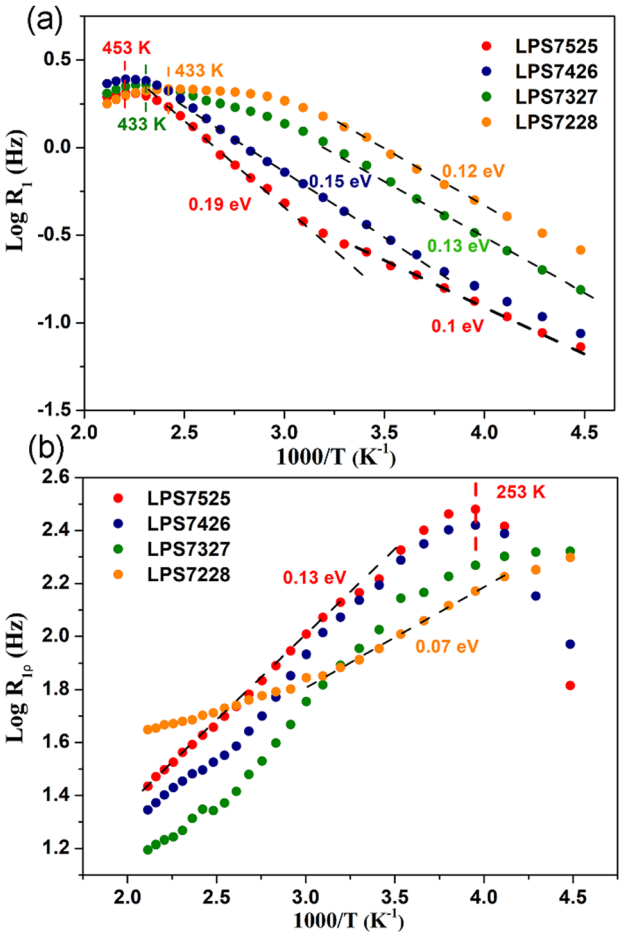

Fig. 6 Temperature dependence of ^{7}Li relaxation rates in the laboratory frame R_1 (a), and in the rotating frame $R_{1\rho}$ (b).

and $R_{1\rho}$ can be expressed by the BPP theory through the following equations:[46,47]

$$R_1 = C_1 \times \left(\frac{\tau}{1+\omega_0^2\tau^2} + \frac{4\tau}{1+4\omega_0^2\tau^2}\right) \quad (1)$$

$$R_{1\rho} = C_2 \times \left(\frac{6\tau}{1+4\omega_1^2\tau^2} + \frac{10\tau}{1+\omega_0^2\tau^2} + \frac{4\tau}{1+4\omega_0^2\tau^2}\right) \quad (2)$$

where C_1 and C_2 are constants related to the interaction strength such as dipolar and quadrupolar interactions; ω_0 and ω_1 are the Larmor frequency and radio frequency field strength, respectively. τ is the correlation time that follows the Arrhenius law $\tau = \tau_0\exp(E_a/(k_BT))$. Plots of $\log(R_1)$, $\log(R_{1\rho})$ *vs.* $1/T$ are typically characterized by maxima where $\omega_{(0|(1))}\tau = 0.616$ (0.5), which means the average motional rates of ions are at or close to the Larmor frequency in the lab frame or the rotating frame. In the low temperature flank, *i.e.* slow motional regime with $\omega_{(0|1)}\tau \gg 1$. Eqn (1) can be reduced to

$$\log R_1 = \log\left(\frac{2C_1}{\omega_0^2}\right) - \log\tau_0 - \frac{0.434E_a}{k} \times \frac{1}{T}.$$

In the high temperature flank, *i.e.* fast motional regime with $\omega_{(0|1)}\tau \ll 1$, eqn (1) can be simplified to

$$\log(R_1) = \log(5C_1) + \log(\tau_0) + \frac{0.434E_a}{k} \times \frac{1}{T}.$$

In this way we can extract the activation energy from the slope of the $\log(R_1)$ *vs.* $1/T$ curves. Fig. 6a shows the temperature dependence of $\log(R_1)$. For β-Li_3PS_4 (LPS7525), two relaxation process are present in the low temperature regime. From 223 K to room temperature (RT, 298 K), $\log(R_1)$ increases linearly with increasing temperature. This process, characterized by an activation energy of 0.1 eV, is ascribed to very fast local motions, *i.e.* vibration of Li ion in the lattice. Above RT, another relaxation process sets in which can be attributed to the local hopping of Li ions between adjacent Li sites. In addition, more Li vacancies and interstitials are formed in this temperature range. The apparent activation energy in this temperature range is 0.19 eV which agrees well with the previously reported values for β-Li_3PS_4.[22,23] In order to gain insights into the relaxation mechanisms, the dipolar (R_{1D}) and quadrupolar (R_{1Q}) contributions to the relaxation rates are evaluated using eqn (1), At the maximum (T = 453 K), $\omega_0\tau = 0.616$ holds. The R_{1D} and R_{1Q} are calculated to be 0.117 s^{-1} and 1.180 s^{-1}, respectively. The calculation details can be found in the supplementary information. The experimental R_1 is, however, 2.039 s^{-1}, indicating the quadrupolar relaxation dominates the process. There is a substantial discrepancy between the calculated and experimental R_1. Beyond the experimental error, the "background" relaxation including paramagnetic impurities induced relaxation is considered to be responsible for the deviation.[48,49] With increasing Al doping levels, the system relaxes faster, indicative of faster motional processes. Upon Al doping, the maxima of $\log R_1$ are shifted to lower temperature (from 453 K to 413 K), providing evidence that the ion mobility has been enhanced. Besides, pronounced changes in relaxation curve shape are observed. The activation energies from the low temperature flank are decreased from 0.19 eV to 0.13 eV upon Al incorporation. For LPS7228, the relaxation rate curves exhibit very broad maxima, which means multiple motional process are present in parallel. Since the domain size in LPS7228 is small, Li ions exchange extremely fast between different domains, therefore, a single T_1 is observed at each temperature. Compared with the SLR data for $Li_7P_3S_{11}$ reported in the literature,[50,51] it is possible that the process characterized by T_{max} at lower temperature represents the second spin reservoir from ^{7}Li spins in $Li_7P_3S_{11}$. At least two motional process were visible in ^{6}Li SLR for $Li_7P_3S_{11}$ reported by Wilkening group.[50] The LPS7228 sample mainly consists of $Li_{2.82}Al_{0.06}PS_4$ and $Li_7P_3S_{11}$ which further broadens the maxima of R_1 relaxation curve. It is challenging to resolve different motional process from ^{7}Li SLR for each component in LPS7228. However, There is no doubt that all types of Li ion motions in $Li_{2.82}Al_{0.06}PS_4$, $Li_7P_3S_{11}$ and their grain boundaries can contribute to the relaxation process.

The $R_{1\rho}$ is employed as a probe of Li ion dynamics in the kHz range that is associated with long-range Li ion diffusion. The measured $R_{1\rho}$ was deconvoluted into a single exponential part and a stretched exponential part. Fig. 6b displays single exponential part $\log R_{1\rho}$ *vs.* $1000/T$. At first glance, it seems that only one motional process is present in β-Li_3PS_4 with an activation barrier of 0.13 eV. Similar activation energies are obtained for LPS7426. It is interesting that a very flat slope appears in LPS7228. An activation energy of 0.07 eV is obtained which was reported for $Li_7P_3S_{11}$ glass ceramics,[50] indicating a much lower barrier for Li ion diffusion in LPS7228. The activation energy determined by NMR is much smaller than the activation energy determined by EIS measurement.[25] This is typical for fast ion conductors because NMR probes Li ion motion at specific frequencies. EIS measurements, on the other hand, reflect an overall Li ion mobility that includes all types of Li ion motion. In most cases, activation energies determined by NMR spin–lattice relaxation are lower than those determined by EIS measurements. With increasing Al doping, the $R_{1\rho}$ maxima are shifting towards lower temperature which is in line with the R_1 measurements. It should be noted that the maximum of $R_{1\rho}$ for LPS7228 is not well pronounced, implying multiple Li ion conduction pathways exist in such multiphasic material.

Li ion diffusion in β-Li_3PS_4 occurs preferably along the b axis through Li2 and Li3 sites. 3D bulk Li ion diffusion is hindered by the limited ion jump between *bc* planes.[52] When a small amount of Al^{3+} dopants are introduced into the lattice as is the case for sample LPS7426, vacancies are created at tetrahedral Li1 sites, facilitating Li ion diffusion through the lattice, increasing the ionic conductivity is enhanced by up to a factor of ~3. Interestingly the activation barrier for Li hopping in the pure β-Li_3PS_4 and the doped $Li_{3-3x}Al_xPS_4$ (LPS7426) are similar.

^{27}Al MAS NMR spectra demonstrate that the maximum content of Al incorporation in β-Li_3PS_4 is around x = 0.06. Upon increasing the Al content in the synthesis mixture, the highest ionic conductivity is obtained for LPS7228 which is very heterogeneous according to the ^{27}Al and ^{31}P MAS NMR spectra as well as the PXRD pattern. Several factors have to be taken into account in interpreting the enhanced ionic conductivities. On one hand, Al incorporation has introduced more vacancies in the crystal structure and promoted the bulk Li ion diffusion. In addition, multiple phases are formed as a result of the synergistic effects of Al incorporation and a shift in the Li_2S/P_2S_5 ratio in the synthesis mixture. A detailed study of the structural evolution of these complicated multiphasic materials, the pathways for the superior Li ion diffusion and their potential application in all-solid-state batteries is described in a separate paper.[25]

4. Conclusions

In summary, we have investigated the impact of Al incorporation on β-Li_3PS_4 from both the structural and dynamics perspective. Based on ^{27}Al and ^{6}Li NMR spectra, we conclude that the Al atoms are embedded into octahedral Li2 (4b) sites while

the vacancies are formed Li1 (8d) sites, facilitating Li ion jumping between *bc* plane. It is found that the maximum incorporation of Al in β-Li_3PS_4 system is approximately x = 0.06. Upon further increase of Al_2S_3 in the synthesis mixture, multiple phases are formed as confirmed by ^{31}P NMR spectra; the Li_2S–P_2S_5–Al_2S_3 system becomes more heterogeneous as is corroborated by both the ^{27}Al NMR spectra and the PXRD experiments. As evidenced by ^{7}Li NMR relaxometry, different efficient Li ion conduction pathway exist as is explored in ref. 25.

Conflicts of interest

There are no conflicts to declare.

Acknowledgements

H. Qu would like to thank the financial support from China Scholarship Council (CSC No. 201804910640). The Netherlands Organisation for Scientific Research (NWO) is greatly acknowledged for the support of the solid-state NMR facility for advanced materials science which is part of the uNMR-NL ROADMAP facilities (NWO project no. 184.035.002). We thank Dr Jennifer Gomez Badillo for her assistance in the double-resonance experiment. Gerrit Janssen, Hans Janssen, and Ruud Aspers are gratefully acknowledged for their technical support.

Notes and references

1 J. B. Goodenough and P. Singh, Review-Solid Electrolytes in Rechargeable Electrochemical Cells, *J. Electrochem. Soc.*, 2015, **162**(14), A2387–A2392.
2 A. Manthiram, X. Yu and S. Wang, Lithium Battery Chemistries Enabled by Solid-State Electrolytes, *Nat. Rev. Mater.*, 2017, **2**(4), 16103.
3 J. C. Bachman, S. Muy, A. Grimaud, H.-H. Chang, N. Pour, S. F. Lux, O. Paschos, F. Maglia, S. Lupart, P. Lamp, L. Giordano and Y. Shao-Horn, Inorganic Solid-State Electrolytes for Lithium Batteries: Mechanisms and Properties Governing Ion Conduction, *Chem. Rev.*, 2016, **116**(1), 140–162.
4 Z. Zhang, Y. Shao, B. Lotsch, Y.-S. Hu, H. Li, J. Janek, L. F. Nazar, C.-W. Nan, J. Maier, M. Armand and L. Chen, New Horizons for Inorganic Solid State Ion Conductors, *Energy Environ. Sci.*, 2018, **11**(8), 1945–1976.
5 R. Kanno, T. Hata, Y. Kawamoto and M. Irie, Synthesis of A New Lithium Ionic Conductor, Thio-LISICON–Lithium Germanium Sulfide System, *Solid State Ionics*, 2000, **130**(1), 97–104.
6 R. Kanno and M. Murayama, Lithium Ionic Conductor Thio-LISICON: The Li_2S–GeS_2–P_2S_5 System, *J. Electrochem. Soc.*, 2001, **148**(7), A742.
7 C. Vinod Chandran and P. Heitjans, One – Solid-State NMR Studies of Lithium Ion Dynamics Across Materials Classes, in *Annual Reports on NMR Spectroscopy*, ed. G. A. Webb, Academic Press, 2016, vol. 89, pp. 1–102.
8 S. Ohno, A. Banik, G. F. Dewald, M. A. Kraft, T. Krauskopf, N. Minafra, P. Till, M. Weiss and W. G. Zeier, Materials Design of Ionic Conductors for Solid State Batteries, *Prog, Energy*, 2020, **2**(2), 022001.
9 D. Liu, W. Zhu, Z. Feng, A. Guerfi, A. Vijh and K. Zaghib, Recent Progress in Sulfide-Based Solid Electrolytes for Li-Ion Batteries, *Mater. Sci. Eng., B*, 2016, **213**, 169–176.
10 R. Kanno, M. Murayama and K. Sakamoto, New Lithium Solid Electrolytes, Thio-LISICON: Materials Design Concept and Application to Solid State Battery, *Solid State Ion.*, 2002, 13–22.
11 N. Kamaya, K. Homma, Y. Yamakawa, M. Hirayama, R. Kanno, M. Yonemura, T. Kamiyama, Y. Kato, S. Hama, K. Kawamoto and A. Mitsui, A Lithium Superionic Conductor, *Nat. Mater.*, 2011, **10**(9), 682–686.
12 P. Bron, S. Johansson, K. Zick, J. Schmedt auf der Günne, S. Dehnen and B. Roling, $Li_{10}SnP_2S_{12}$: An Affordable Lithium Superionic Conductor, *J. Am. Chem. Soc.*, 2013, **135**(42), 15694–15697.
13 A. Kuhn, O. Gerbig, C. Zhu, F. Falkenberg, J. Maier and B. V. Lotsch, A New Ultrafast Superionic Li-Conductor: Ion Dynamics in $Li_{11}Si_2PS_{12}$ and Comparison with Other Tetragonal LGPS-type Electrolytes, *Phys. Chem. Chem. Phys.*, 2014, **16**(28), 14669–14674.
14 B. Karasulu, S. P. Emge, M. F. Groh, C. P. Grey and A. J. Morris, Al/Ga-Doped $Li_7La_3Zr_2O_{12}$ Garnets as Li-Ion Solid-State Battery Electrolytes: Atomistic Insights into Local Coordination Environments and Their Influence on ^{17}O, ^{27}Al, and ^{71}Ga NMR Spectra, *J. Am. Chem. Soc.*, 2020, **142**(6), 3132–3148.
15 H. Aono, E. Sugimoto, Y. Sadaoka, N. Imanaka and G. Y. Adachi, Ionic Conductivity of the Lithium Titanium Phosphate ($Li_{1+X}M_X$-$Ti_{2-X}(PO_4)_3$, M = Al, Sc, Y, and La) Systems, *J. Electrochem. Soc.*, 1989, **136**(2), 590–591.
16 J. S. Thokchom, N. Gupta and B. Kumar, Superionic Conductivity in a Lithium Aluminium Germanium Phosphate Glass–Ceramic, *J. Electrochem. Soc.*, 2008, **155**(12), A915.
17 S. P. Ong, Y. Mo, W. D. Richards, L. Miara, H. S. Lee and G. Ceder, Phase Stability, Electrochemical Stability and Ionic Conductivity of the $Li_{10\pm1}MP_2X_{12}$ (M = Ge, Si, Sn, Al or P, and X = O, S or Se) Family of Superionic Conductors, *Energy Environ. Sci.*, 2013, **6**(1), 148–156.
18 P. Zhou, J. Wang, F. Cheng, F. Li and J. Chen, A Solid Lithium Superionic Conductor $Li_{11}AlP_2S_{12}$ with a Thio-LISICON Analogous Structure, *Chem. Commun.*, 2016, **52**(36), 6091–6094.
19 C. Dietrich, D. A. Weber, S. J. Sedlmaier, S. Indris, S. P. Culver, D. Walter, J. Janek and W. G. Zeier, Lithium Ion Conductivity in Li_2S–P_2S_5 Glasses – Building Units and Local Structure Evolution During the Crystallization of Superionic Conductors Li_3PS_4, $Li_7P_3S_{11}$ and $Li_4P_2S_7$, *J. Mater. Chem. A*, 2017, **5**(34), 18111–18119.
20 Ö. U. Kudu, T. Famprikis, B. Fleutot, M.-D. Braida, T. Le Mercier, M. S. Islam and C. Masquelier, A Review of Structural Properties and Synthesis Methods of Solid Electrolyte Materials in the Li_2S–P_2S_5 Binary System, *J. Power Sources*, 2018, **407**, 31–43.
21 M. Tachez, J.-P. Malugani, R. Mercier and G. Robert, Ionic Conductivity of and Phase Transition in Lithium Thiophosphate Li_3PS_4, *Solid State Ionics*, 1984, **14**(3), 181–185.
22 H. Stöffler, T. Zinkevich, M. Yavuz, A. Senyshyn, J. Kulisch, P. Hartmann, T. Adermann, S. Randau, F. H. Richter, J. Janek

and S. Indris, Ehrenberg, H. Li^+-Ion Dynamics in β-Li_3PS_4 Observed by NMR: Local Hopping and Long-Range Transport, *J. Phys. Chem. C*, 2018, **122**(28), 15954–15965.

23 D. Prutsch, B. Gadermaier, H. Brandstätter, V. Pregartner, B. Stanje, D. Wohlmuth, V. Epp, D. Rettenwander, I. Hanzu and H. M. R. Wilkening, Nuclear Spin Relaxation in Nanocrystalline β-Li_3PS_4 Reveals Low-Dimensional Li Diffusion in an Isotropic Matrix, *Chem. Mater.*, 2018, **30**(21), 7575–7586.

24 J. H. Kennedy, C. Schaupp, H. Eckert and M. Ribes, Aluminium Substitution in the Glass System $0.33[(1-x)P_2S_5-xAl_2S_3]-0.67Li_2S$, *Solid State Ionics*, 1991, **45**(1), 21–27.

25 Y. Wang, H. Qu, B. Liu, X. Li, J. Ju, S. Zhang, J. Ma, C. Li, Z. Hu, C.-K. Chang, H.-S. Sheu, L. Cui, F. Jiang, E. R. H. van Eck, A. P. M. Kentgens, G. Cui and L. Chen, Self-Organized Hetero-Nanodomains Actuating Super Li^+ Conduction in Glass Ceramics, *Nat. Commun.*, 2023, DOI: **10.1038/s41467-023-35982-7**.

26 K. Momma and F. Izumi, VESTA 3 for Three-Dimensional Visualization of Crystal, Volumetric and Morphology Data, *J. Appl. Crystallogr.*, 2011, **44**(6), 1272–1276.

27 S. G. J. van Meerten, W. M. J. Franssen and A. P. M. Kentgens, ssNake: A Cross-Platform Open-Source NMR Data Processing and Fitting Application, *J. Magn. Reson.*, 2019, **301**, 56–66.

28 H. Stöffler, T. Zinkevich, M. Yavuz, A.-L. Hansen, M. Knapp, J. Bednarčík, S. Randau, F. H. Richter, J. Janek, H. Ehrenberg and S. Indris, Amorphous versus Crystalline Li_3PS_4: Local Structural Changes during Synthesis and Li Ion Mobility, *J. Phys. Chem. C*, 2019, **123**(16), 10280–10290.

29 Y. Seino, M. Nakagawa, M. Senga, H. Higuchi, K. Takada and T. Sasaki, Analysis of the Structure and Degree of Crystallisation of $70Li_2S$–$30P_2S_5$ Glass Ceramic, *J. Mater. Chem. A*, 2015, **3**(6), 2756–2761.

30 S. Neuberger, S. P. Culver, H. Eckert, W. G. Zeier and J. Schmedt auf der Günne, Refinement of the Crystal Structure of $Li_4P_2S_6$ Using NMR Crystallography, *Dalton Trans.*, 2018, **47**(33), 11691–11695.

31 S. M. Martin and J. A. Sills, ^{29}Si and ^{27}Al MASS-NMR Studies of Li_2S + Al_2S_3 + SiS_2 Glasses, *J. Non-Cryst. Solids*, 1991, **135**(2), 171–181.

32 A. Lafond, X. Rocquefelte, M. Paris, C. Guillot-Deudon and V. Jouenne, Crystal Chemistry and Electronic Structure of the Photovoltaic Buffer Layer, $(In_{1x}Al_x)_2S_3$, *Chem. Mater.*, 2011, **23**(23), 5168–5176.

33 M. Haouas, F. Taulelle and C. Martineau, Recent Advances in Application of ^{27}Al NMR Spectroscopy to Materials Science, *Prog. Nucl. Magn. Reson. Spectrosc.*, 2016, **94–95**, 11–36.

34 T. Gullion and J. Schaefer, Rotational-Echo Double-Resonance NMR, *J. Magn. Reson.*, 1989, **81**(1), 196–200.

35 S. Ohno, T. Bernges, J. Buchheim, M. Duchardt, A.-K. Hatz, M. A. Kraft, H. Kwak, A. L. Santhosha, Z. Liu, N. Minafra, F. Tsuji, A. Sakuda, R. Schlem, S. Xiong, Z. Zhang, P. Adelhelm, H. Chen, A. Hayashi, Y. S. Jung, B. V. Lotsch, B. Roling, N. M. Vargas-Barbosa and W. G. Zeier, How Certain Are the Reported Ionic Conductivities of Thiophosphate-Based Solid Electrolytes? An Interlaboratory Study, *ACS Energy Lett.*, 2020, **5**(3), 910–915.

36 P. Adeli, J. D. Bazak, A. Huq, G. R. Goward and L. F. Nazar, Influence of Aliovalent Cation Substitution and Mechanical Compression on Li-Ion Conductivity and Diffusivity in Argyrodite Solid Electrolytes, *Chem. Mater.*, 2021, **33**(1), 146–157.

37 R. Bertermann and W. Müller-Warmuth, Universality of NMR Results in LISICON Systems and Other Solid Lithium Conductors, *Z. Naturforsch., A: Phys. Sci.*, 1998, **53**(10–11), 863–873.

38 K. Volgmann, V. Epp, J. Langer, B. Stanje, J. Heine, S. Nakhal, M. Lerch, M. Wilkening and P. Heitjans, Solid-State NMR to Study Translational Li Ion Dynamics in Solids with Low-Dimensional Diffusion Pathways, *Z. Phys. Chem.*, 2017, **231**(7–8), 1215–1241.

39 V. Epp and M. Wilkening, Li-ion Dynamics in Solids as Seen Via Relaxation NMR, *Handbook of Solid State Batteries*, 2015, pp. 133–190.

40 P. Heitjans, A. Schirmer and S. Indris, NMR and β-NMR Studies of Diffusion in Interface-Dominated and Disordered Solids, in *Diffusion in Condensed Matter: Methods, Materials, Models*, ed. P. Heitjans and J. Kärger, Springer Berlin Heidelberg, Berlin, Heidelberg, 2005, pp. 367–415.

41 A. Kuhn, P. Sreeraj, R. Pöttgen, H.-D. Wiemhöfer, M. Wilkening and P. Heitjans, Li Ion Diffusion in the Anode Material $Li_{12}Si_7$: Ultrafast Quasi-1D Diffusion and Two Distinct Fast 3D Jump Processes Separately Revealed by ^7Li NMR Relaxometry, *J. Am. Chem. Soc.*, 2011, **133**(29), 11018–11021.

42 J. R. Hendrickson and P. J. Bray, A Phenomenological Equation for NMR Motional Narrowing in Solids, *J. Magn. Reson.*, 1973, **9**(3), 341–357.

43 M. Uitz, V. Epp, P. Bottke and M. Wilkening, Ion Dynamics in Solid Electrolytes for Lithium Batteries, *J. Electroceram.*, 2017, **38**(2), 142–156.

44 P. Heitjans, S. Indris and M. Wilkening, Solid-State Diffusion and NMR, 2005.

45 K. Hayamizu, Y. Terada, K. Kataoka, J. Akimoto and T. Haishi, Relationship Between Li^+ Diffusion and Ion Conduction for Single-Crystal and Powder Garnet-Type Electrolytes Studied by ^7Li PGSE NMR Spectroscopy, *Phys. Chem. Chem. Phys.*, 2019, **21**(42), 23589–23597.

46 N. Bloembergen, E. M. Purcell and R. V. Pound, Relaxation Effects in Nuclear Magnetic Resonance Absorption, *Phys. Rev.*, 1948, **73**(7), 679–712.

47 A. F. McDowell, N. L. Adolphi and C. A. Sholl, Site and Barrier Energy Distributions That Govern the Rate of Hydrogen Motion in Quasicrystalline $Ti_{45}Zr_{38}Ni_{17}H_x$, *J. Phys.: Condens. Matter*, 2001, **13**(43), 9799–9812.

48 M. Wilkening and P. Heitjans, Li Jump Process in h-$Li_{0.7}TiS_2$ Studied by Two-Time ^7Li Spin-Alignment Echo NMR and Comparison with Results on Two-Dimensional Diffusion From Nuclear Magnetic Relaxation, *Phys. Rev. B: Condens. Matter Mater. Phys.*, 2008, **77**(2), 024311.

49 P. M. Richards, Nuclear Magnetic Relaxation by Paramagnetic Impurities in Superionic Conductors, *Phys. Rev. B: Condens. Matter Mater. Phys.*, 1978, **18**(11), 6358–6371.

50 D. Wohlmuth, V. Epp and M. Wilkening, Fast Li Ion Dynamics in the Solid Electrolyte $Li_7P_3S_{11}$ as Probed by ^{6,7}Li NMR Spin–Lattice Relaxation, *Chem. Phys. Chem.*, 2015, **16**(12), 2582–2593.
51 C. Yu, S. Ganapathy, E. R. H. van Eck, L. van Eijck, N. de Klerk, E. M. Kelder and M. Wagemaker, Investigation of Li-ion transport in $Li_7P_3S_{11}$ and solid-state lithium batteries, *J. Energy Chem.*, 2019, **38**, 1–7.
52 N. J. J. de Klerk, E. van der Maas and M. Wagemaker, Analysis of Diffusion in Solid-State Electrolytes through MD Simulations, Improvement of the Li-Ion Conductivity in β-Li_3PS_4 as an Example, *ACS Appl. Energy Mater.*, 2018, **1**(7), 3230–3242.